Confined Element Distribution with Structure-Driven Energy Coupling for Enhanced Prussian Blue Analogue Cathode

*Xinyu Hu, Weishun Jian, Ningyun Hong, Xue Zhong, Mushi Yang, Shusheng Tao, Jiangnan Huang, Haoji Wang, Jingqiang Gao, Wentao Deng, Guoqiang Zou, Hongshuai Hou, Debbie S. Silvester, Craig E. Banks, and Xiaobo Ji**

Abstract: The structural failure of $Na_2Mn[Fe(CN)_6]$ could not be alleviated with traditional modification strategies through the adjustable composition property of Prussian blue analogues (PBAs), considering that the accumulation and release of stress derived from the MnN_6 octahedrons are unilaterally restrained. Herein, a novel application of adjustable composition property, through constructing a coordination competition rela- tionship between chelators and $[Fe(CN)_6]^{4-}$ to direction-ally tune the enrichment of elements, is proposed to restrain structural degradation and induce unconven- tional energy coupling phenomenon. The non-uniform distribution of elements at the M_1 site of PBAs (NFM- PB) is manipulated by the sequentially precipitated Ni, Fe, and Mn according to the Irving-William order. Electrochemically active Fe is operated to accompany Mn, and zero-strain Ni is modulated to enrich at the surface, synergistically mitigating with the enrichment and release of stress and then significantly improving the structural stability. Furthermore, unconventional energycoupling effect, a fusion of the electrochemical behaviorbetween Fe_{LS} and Mn_{HS}, is triggered by the confined element distribution, leading to the enhanced electro- chemical stability and anti-polarization ability. Conse-quently, the NFM-PB demonstrates superior rate per- formance and cycling stability. These findings further exploit potentialities of the adjustable composition property and provide new insights into the component design engineering for advanced PBAs.

[*] X. Hu, W. Jian, N. Hong, X. Zhong, M. Yang, S. Tao, J. Huang, H. Wang, J. Gao, W. Deng, G. Zou, H. Hou, X. Ji
State Key Laboratory of Powder Metallurgy, College of Chemistry and Chemical Engineering, Central South University, Changsha, 410083, China
E-mail: xji@csu.edu.cn

D. S. Silvester
School of Molecular and Life Sciences, Curtin University, GPO Box U1987, Perth, Western Australia 6845, Australia

C. E. Banks
Faculty of Science and Engineering, Manchester Metropolitan University, Manchester, M1 5GD UK

Introduction

Prussian blue analogues (PBAs), denoted as $A_xM_1[M_2-(CN)_6]_{1-y}\&_y{\cdot}nH_2O$ (: alkali ions, M_1/M_2: transition metal ions, &: vacancy of $[M_2(CN)_6]$), are candidates for cathode of sodium-ion batteries (SIBs) due to their open ion diffusion pathways and adjustable composi- tion property.[1] Their adjustable composition property is recognized as the structural basis for performance optimiza- tion. A series of homogeneous cathodes with single or multiple elements uniformly distributed at the M_1 site have been reported, employing $Na_4[Fe(CN)_6]$ and different divalent transition metal ions (e.g., Mn, Fe, Ni, Cu, and Zn) as raw materials.[2] Located in the M_1 site, Mn and Fe are electrochemically active, while Ni, Cu, and Zn are electro- chemically inert.[3]

When only one active element exists at the M_1 site, although $Na_2Mn[Fe(CN)_6]$ and $Na_2Fe[Fe(CN)_6]$ both exhibit a remarkable theoretical capacity of 170 mAh/g based on a two-electron redox reaction, they respectively face severe structural degradation and low practical capacity.[4] Generally, other transition metal elements are introduced into the M_1 site to increase the capacity of $Na_2Fe[Fe(CN)_6]$ by enhancing the reactivity of Fe at the M_2 site.[5] However, the capacity fading of $Na_2Mn[Fe(CN)_6]$ cannot be solved by this strategy in the long term, unless a large number of elements without the Jahn–Teller effect are employed, since the stress originated from the MnN_6 octahedra cannot be avoided during the charge/discharge process.[6] PBAs with five kinds of M_1 site elements, a high-entropy material, performs satisfactory cycling stability.[7] However, only a small number of guest ions can be stored in lattices because a large number of inert elements is used.[8] It is particularly important to further utilize the adjustable composition property of PBAs and expand its modification boundary for promoting the commercial application of PBAs.

PBAs is typically prepared though co-precipitation reaction in which a rapid nucleation process brings in $[Fe(CN)_6]$ vacancies and coordinated water.[9] Therefore, it is of great significance to retard the nucleation process for the preparation of PBAs with a perfect structure. Addition of chelator (such as sodium citrate ($C_6H_5Na_3O_7$)) is considsered to be the most successful chemical solution to manipulate the nucleation kinetics through constructing a competitive relationship between chelating agents and $[Fe-(CN)_6]^{4-}$.[10] The growth process of $Na_2Mn[Fe(CN)_6]$ underhe influence of $C_6H_5Na_3O_7$ was chosen as an example: the precipitation reaction between $[Fe(CN)_6]^{4-}$ and Mn^{2+} can only occur after the dissociation of [Mn^{2+}-citrate] when Mn^{2+} was coordinated by $C_6H_5Na_3O_7$ through O to form a stable chelate [Mn^{2+}-citrate].[11] At this moment, $C_6H_5Na_3O_7$ acts as a sustained-release agent and the nucleation rate of $Na_2Mn[Fe(CN)_6]$ depends on the rate of [Mn^{2+}-citrate] dissociation, i.e., the stability of the complex, since the solubility product constant of the precipitate is much smaller than the stability constant of the complex. Importantly, the Irving-William order (i.e., $Mn^{2+} < Fe^{2+} < Co^{2+} < Ni^{2+} < Cu^{2+} > Zn^{2+}$) reflects the stability order of complexes generated by transition metal ions in the fourth period and ligands containing O or N coordination atoms.[12] The dissociation

sequence of [TM-citrate] is well consistent with the Irving-William order in an aqueous solution containing sodium citrate and various fourth-period transition metal ions. In this situation, the nucleation rate of $Na_2Mn[Fe(CN)_6]$ and the precipitation sequence of transition metal ions are dominated by $C_6H_5Na_3O_7$. Therefore, with the influence of coordination and competition reaction, a confined distribution of elements at the M_1 site of PBAs might be achieved instead of a uniform distribution, which is a new application form of the adjustable composition property of PBAs.

The correlation between Jahn–Teller effect of Mn^{3+} and capacity fading of $Na_2Mn[Fe(CN)_6]$ was extensively studied where the MnN_6 octahedra would expand and contract, and then internal stress shall generated due to the transformation of Mn^{2+} ($3d^5$)/Mn^{3+}($3d^4$) during the charge/discharge process.[13] The localized stress enrichment and release is induced by the continuous deformation of MnN_6 octahedrons, macroscopically manifested as particle deformation and cracks.[14] Therefore, it is crucial to suppress the stress enrichment and solidify the crystal structure for prolonging the service life of $Na_2Mn[Fe(CN)_6]$. In this work, a cathode (NFM-PB-1) with non-uniform distribution of elements at the M_1 site was successfully prepared by achieving a coordination competition relationship between chelators and $[Fe(CN)_6]^{4-}$, which is a novel application of adjustable composition property. In the non-homogeneous reaction, due to the sequentially precipitated Ni, Fe, and Mn according to the Irving-William order, electrochemically active Fe without Jahn–Teller effect is selected to accompany Mn to balance stress distribution, and zero-strain Ni is enriched on the particle surface to inhibit stress release, which synergistically mitigates with the enrichment and release of stress and then considerably improves the structural stability. Meanwhile, in the first charge/discharge process, a thorough energy coupling effect, a fusion of the electrochemical behavior between Fe_{LS} and Mn_{HS}, was mediated by the confined element distributions, displaying an enhanced electrochemical stability, anti-polarization ability, and guest ion diffusion, compared with the energy coupling effect induced by water electrolysis. In consequence, NFM-PB-1 with confined element distribution exhibits a longer cycle life and superior rate performance during cell voltage cycling of 2.0–4.2 V.

Results and Discussion

The confined element distribution at the M_1 site of PBAs is successfully achieved by employing the confined element strategy based on the Irving–Williams order (i.e., Mn^{2+} $<Fe^{2+}$ $<Co^{2+}$ $<$ Ni^{2+} $<Cu^{2+}$ $>Zn^{2+}$), as depicted in Figure 1a.In order to verify the applicability of the Irving-William order, the binding strengths of citrate with various transitionmetals were assessed utilizing density functional theory (DFT). As the number of d electrons in the central atom are increased, the binding energy of the complex gradually rises(Figure 1b). Evidently, the stability order of complexes
formed by citrate and transition metal ions (Mn^{2+}, Fe^{2+}, and Ni^{2+}) follows the sequence [Ni^{2+}-citrate] >[Fe^{2+}-citrate] > [Mn^{2+}-citrate], in good accordance with the Irving–Williams order. Apparently, the nucleation rate of PBAs and the precipitation sequence of transition metal ions are determined by $C_5H_7O_5COO^{3-}$. When $C_5H_7O_5COO^{3-}$ and $[Fe(CN)_6]^{4-}$ coexist, there will be a competition among transition metal ions. The stability constant of the soluble [TM-citrate] is much larger than the solubility product constant of the insoluble PBAs in a liquid phase. Therefore, the stability constant of the [TM-citrate] is identified as a critical factor in affecting the precipitation sequence of PBAs, rather than the solubility product constant of PBAs.

To evaluate the practicality of confined element strategy, homogeneous cathodes (NFM-PB) containing Mn, Fe, and Ni was obtained through one-step co-precipitation assisted by sodium citrate. The samples exhibit typical cubic crystallographic characteristics (Fm-3 m) and microstructures (Figures S1 and S2). The lattice parameters of Mn-PB (M-PB) and NFM-PB-1 were analyzed using powder X-ray diffraction (XRD) by Rietveld refinement on FULLPROF software, as shown in Figures 1c and 1d, respectively. NFM-PB-1 is imparted with enhanced crystallinity and reduced lattice parameters after introducing of Fe^{2+} and Ni^{2+}, owing to slower nucleation rate and smaller ionic radii (Table S1). Compared to M-PB, a smaller interplanar spacing is observed in the exterior of NFM-PB-1 (Figures 1e–h). Simultaneously, the average particle size of the cathodes is reduced, benefited from the sustained-release function of $C_6H_5Na_3O_7$. Fe and Mn elements are uniformly distributed within M-PB (Figure 1i). Furthermore, the signal intensity of Mn is slightly higher than that of Fe, which could be attributed to the $[Fe(CN)_6]$ vacancy (Figure 1k). According to Figures S3 and S4, non-uniform distribution of elements at M_1 site is detected in NM-PB and NFM-PB-0. It is found that Ni and Mn elements are enriched in the surface and bulk phase of NM-PB, respectively. In NFM-PB-0, regarding the element located at the M_1 site, it is Fe on the surface while it is Fe and Mn inside the bulk with a uniform distribution. The presence of Fe at M_1 site is suggested by the prominent Fe signal (Figure 1l). At the end of the reaction, Ni^{2+} in the [Ni^{2+}-citrate] is slowly released and then nucleated epitaxially on the crystal surface, which contribute to Fe enrichment, located at the M_1 site on the surface, conversing to Ni and Fe co-enrichment, as shown in Figures 1j and 1l. Therefore, NFM-PB-1 is a cathode with a confined distribution of three elements (Ni, Fe, and Mn),

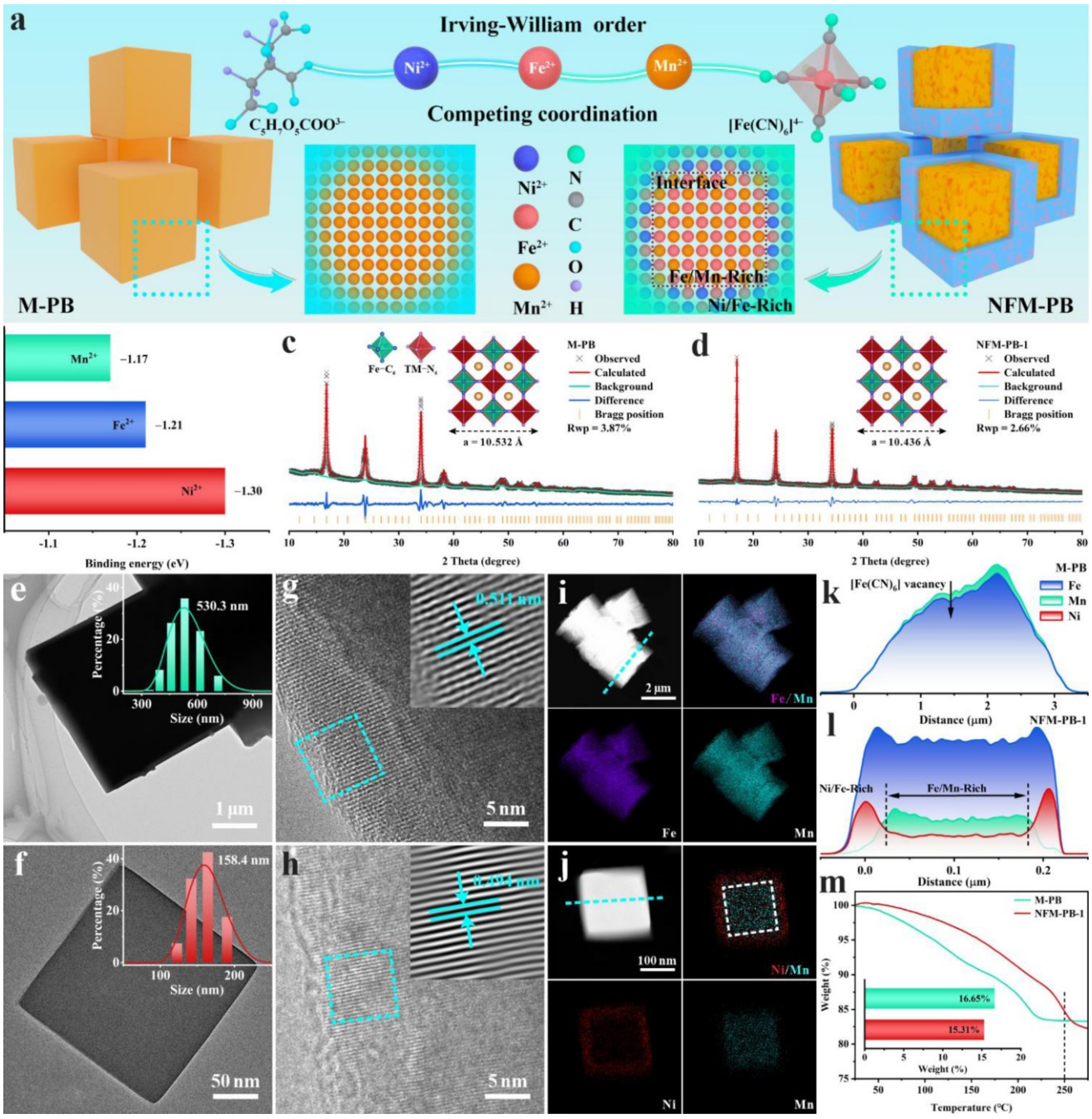

Figure 1. Structural characterization and synthesis mechanism. a) Schematic illustration of the synthesis mechanism for the M-PB and NFM-PB. b) The binding energy of [TM-citrate] (TM=Ni, Fe, and Mn). The Rietveld refinement of XRD patterns of (c) M-PB and (d) NFM-PB-1. TEM with inset particle size distribution of (e) M-PB and (f) NFM-PB-1. HRTEM images of (g) M-PB and (h) NFM-PB-1. i) EDS element mappings and (k) line-scan result of M-PB. j) EDS element mappings and (l) line-scan result of NFM-PB-1. m) TGA curves.

which explains the contraction of the lattice at the cathode surface. The attractive disparities in element enrichment should come from the synergistic action of coordination chemistry and competitive reaction. In addition, the element enrichment boundary is not able to distinctly distinguish, given the consistent framework units and the similar ionic radii.

Thermogravimetric analysis (TGA) results revealed that the water content of M-PB and NFM-PB-1 is determined to be 16.65 wt% and 15.31 wt%, respectively (Figures 1m and S5). According to the results of Inductively Coupled Plasma-Mass Spectrometry (ICP- MS), the chemical formu- las of the samples are noted as $Na_{1.88}Mn_{1.00}[Fe(CN)_6]_{0.90}$ for M-PB and $Na_{1.77}Ni_{0.04}Fe_{0.48}Mn_{0.48}[Fe(CN)_6]_{0.92}$ for NFM-PB-1 (Table S2). The Ni content in the samples with Ni is lower than the theorized ones, which is thought to be another consequence of the ligand competition relationship under the effect of Irving-William order. The surface elemental

information of Prussian blue analogues was collected utilizing X-ray photoelectron spectroscopy (XPS) and soft X-ray absorption spectroscopy (sXAS) (Figures S6–8). Unlike M-PB with a pronounced Mn signal, weak Mn signals are detected on the surface of NFM-PB-1, indicating that the Mn element is much more enriched in the interior rather than on the surface. Furthermore, in the cathodes both Ni and Mn exist in + 2 valence state, while Fe exists in both + 2 and + 3 valences state due to the natural oxidation of exogenous iron in the environment. The partial oxidation of iron is further justified by Mössbauer spectroscopy (Figure S9). The high-resolution N 1s spectra displays characteristic peaks of X–N (X=Ni, Fe, and Mn) in Figure S7d. The binding energy of X–N undergoes a variation from 397.29 eV (M-PB) to 397.40 eV (NFM-PB-1), which may be attributed to the charge redistribution of —CΞN—.

The cyclic voltammetry (CV) curves at 0.1 mV/s of the as-prepared samples were compared to investigate the impact of confined element distribution, as depicted in Figures 2a and S10. Two redox pairs are observed at ◆3.52/3.12 V and ◆ 3.75/3.52 V for M-PB, corresponding to the transitions of $Mn^{2+}{}_{HS}/Mn^{3+}{}_{HS}$ and $Fe^{2+}{}_{LS}/Fe^{3+}{}_{LS}$, respectively.[15] HS and LS are used to label the high-spin and low-spin states of the ions, respectively. When Ni^{2+} is enriched on the surface, the redox potential of $Mn^{2+}{}_{HS}/Mn^{3+}{}_{HS}$ is shifted to ◆3.57/3.19 V, accompanied with the disappearance of the oxidation peak and attenuation of reduction peak of $Fe^{2+}{}_{LS}$. When Fe^{2+} and Mn^{2+} are precipitated together, the redox peaks belonging to Mn_{HS} and Fe_{LS} are merged as a single peak, which is also discerned in the CV curves of NFM-PB-1 and NFM-PB-2. In particular, the polarization of coupling redox peaks in NFM-PB-1 (0.14 V) is significantly smaller than that of $Mn^{2+}{}_{HS}$/

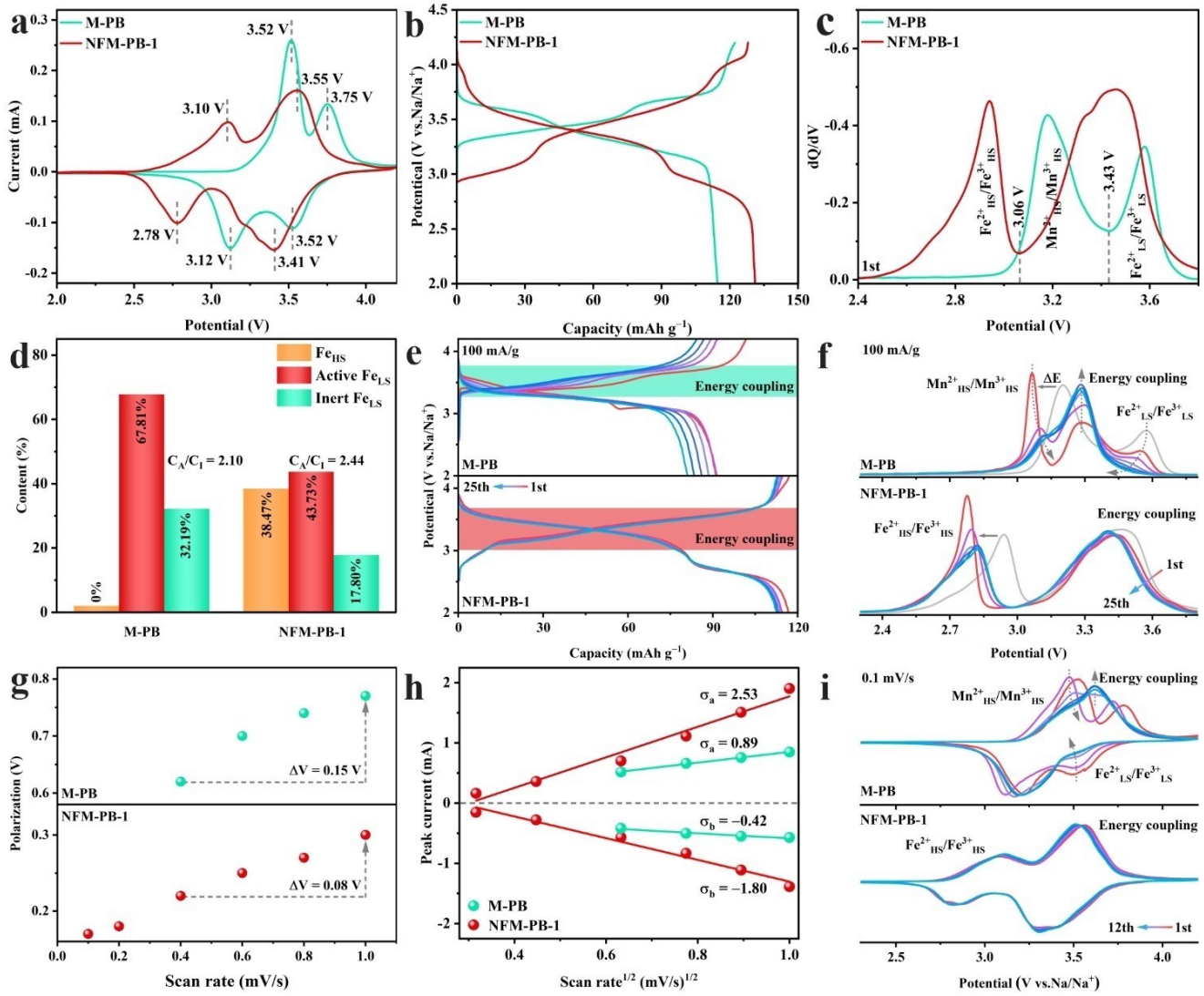

Figure 2. Comparison of energy coupling effect. a) CV curves at 0.1 mV/s. b) The initial charge/discharge curves at 10 mA/g. c) dQ/dV profiles of discharge process at first cycle. d) Electrochemical activity analysis of Fe. e) Galvanostatic charge/discharge curves at different cycles. f) dQ/dV profiles of discharge processes at different cycles. g) Polarization of the energy coupling peak at different scan rates. h) $I_P/\upsilon^{1/2}$ profiles of the energy coupling peak. i) CV curves at different cycles.

Mn^{3+}_{HS} (0.40 V) and $Fe^{2+}_{LS}/Fe^{3+}_{LS}$ (0.23 V) before the coupling. Besides, the redox pair at ~2.78 V is attributed to the $Fe^{2+}_{HS}/Fe^{3+}_{HS}$ for NFM-PB-1.[16] The scope of influence from the energy coupling effect is confined to $Mn^{2+}_{HS}/Mn^{3+}_{HS}$ and $Fe^{2+}_{LS}/Fe^{3+}_{LS}$, without involving with the $Fe^{2+}_{HS}/Fe^{3+}_{HS}$, as evidenced by the negligible alteration in the potential difference of main peak (from 0.30 V to 0.32 V) according to Figure S11. The energy coupling effect can also be observed in the initial charge/discharge curves and dQ/dV profiles of NFM-PB (Figures 2b, 2c, S12, and S13).

The capacity composition of the cathodes during the initial discharge process was analyzed to comprehend the role of metal ions, with the supplement of charge/discharge curves and dQ/dV profiles. As depicted in Figure S14, the capacity contributed by $Fe^{2+}_{LS}/Fe^{3+}_{LS}$ decreases from 40.8 mAh/g (M-PB) to 31.3 mAh/g (NM-PB), owing to the presence of epitaxial Ni-PB. A similar phenomenon is also noticed in its CV curves, where the redox pair of $Fe^{2+}_{LS}/Fe^{3+}_{LS}$ are largely diminished. Clearly, the electrochemical activity of Fe_{LS} is inhibited by the Ni^{2+} that cannot participate in sodium ion (de)intercalation. For NFM-PB, the capacity provided by the coupling platform displays an initial increase followed by a subsequent decrease with the increase of Ni^{2+} content. The influence of Ni^{2+} on capacity can be summarized as two contradictory effects. When the trace amounts of Ni are present in the lattice, the oxidation of Fe^{2+}_{LS} becomes more favorable, as the charge distribution of the crystal framework may be altered.[17] On the other hand, a decline in capacity is induced by inert Ni due to the reduction of active components (Fe_{HS} and Mn_{HS}). Furthermore, the reversible conversion of Fe^{2+}/Fe^{3+} is seriously hindered when the Mn site is vastly occupied by Ni, manifesting as a decreased capacity contribution of $Fe^{2+}_{LS}/Fe^{3+}_{LS}$ (NM-PB). In addition, the discharge specific capacity is increased by Fe_{HS} through enhancing Fe_{LS} activity (from 114.6 mAh/g (M-PB) to 123.4 mAh/g (NFM-PB-0)). In the Fourier transforms of the Fe K-edge EXAFS spectra (Figure S15), the shortening of the Fe—C bond is ascribed to the weakening of the FeC_6 octahedral ligand field driven by the Ni_{HS} and Fe_{HS}, which facilitated the enhanced Fe_{LS} activity and the discharge specific capacity (from 114.6 mAh/g (M-PB) to 131.0 mAh/g (NFM-PB-1)).[18]

The energy coupling phenomenon was always perceived in Mn-PB without H_2O transformed from Mn-PB with H_2O through thermal dehydration. Meanwhile, a gradually emerging energy coupling phenomenon was also detected in the Mn-PB with H_2O as the coordinated water was continuously consumed.[19] The merging of the redox pairs of $Fe_{LS}^{2+}/Fe_{LS}^{3+}$ and $Mn_{HS}^{2+}/Mn_{HS}^{3+}$ is induced by water electrolysis due to the weakened ligand field stabilization energy (LFSE), which can be assessed by contrasting the electrochemical behavior of the cathodes before and after heat treatment.[20] However, the coupling of $Fe_{LS}^{2+}/Fe_{LS}^{3+}$ and $Mn_{HS}^{2+}/Mn_{HS}^{3+}$ is often finite in the first three cycles or occurs after the cathode has been cycled for several times. Prior to electrochemical testing, NFM-PB-1 with 15.31 wt% H_2O was certified as a water-rich phase (Figure 1m). However, a pronounced coupling phenomenon was discovered in the initial charge/discharge process of NFM-PB-1, suggesting an unconventional trigger for energy coupling. According to Figures S10–13, it can be determined that Fe^{2+}_{HS} leads to the formation of coupling effects. For NFM-PB-0, Fe^{2+}_{HS} is uniformly distributed in the whole crystal, while Mn^{2+}_{HS} is enriched in the interior. Therefore, NFM-PB-0 can be considered as equivalent to Fe-substituted Mn-PB with a Fe-PB coating layer, rather than Fe-substituted Mn-PB (FeMn-PB). Uniformly distributed Fe and Mn are observed in the cubic FeMn-PB (Figures S16 and S17). A comparison of the dQ/dV curves of NFM-PB-0 and FeMn-PB is helpful to understand the origin of the unconventional energy coupling effect (Figure S18). Interestingly, the electrochemical characterization of $Mn^{2+}_{HS}/Mn^{3+}_{HS}$ and $Fe^{2+}_{LS}/Fe^{3+}_{LS}$ in FeMn-PB is consistent with that of Mn-PB (M-PB), demonstrating that the energy coupling phenomenon is correlated with the confined distribution of elements at the M_1 site.

It should be emphasized that the reaction electrochemical potential of $Fe^{2+}_{LS}/Fe^{3+}_{LS}$ would be shifted towards lower potentials when the energy coupling of $Mn^{2+}_{HS}/Mn^{3+}_{HS}$ and $Fe^{2+}_{LS}/Fe^{3+}_{LS}$ occurs. In other words, the conversion of $Fe^{2+}_{LS}/Fe^{3+}_{LS}$ becomes much easier, implying more Na^+ can be stored/released. The coupling platform of the NFM-PB-1 releases a specific capacity of 86.9 mAh/g, which stands as the highest among all cathodes. Due to the coupling effect and Fe_{HS}, the electrochemical behavior of Fe_{LS} cannot be distinguished through electrochemical techniques. The valence state information of Fe at different states was characterized by XPS spectra of Fe 2p (Figure S19). When cathodes were deeply oxidized (4.2 V), the signal peaks of Fe^{2+} and Fe^{3+} are perceived on the surfaces of M-PB and NFM-PB-1. The signal of Fe^{2+} is attributed to the inert Fe^{2+}_{LS} that cannot react, while the signal of Fe^{3+} originates in the oxidation of Fe^{2+}_{HS} and active Fe^{2+}_{LS}. Upon discharging to 3.4 V, only the peak corresponding to Fe^{2+} is observed in M-PB. However, when NFM-PB-1 was discharged to 3.1 V, the Fe^{2+} and Fe^{3+} at the surface are associated with Fe^{2+}_{LS} and Fe^{3+}_{HS}, respectively. In addition, only the signal of Fe^{2+} is detected at 2.0 V. The composition of Fe species is determined based on the relative peak areas at different states, as depicted in Figure 2d. In M-PB, 67.81 % of Fe^{2+}_{LS} is participated in the redox, and the ratio of active Fe^{2+}_{LS} to inert Fe^{2+}_{LS} (C_A/C_I) is 2.10. The C_A/C_I value for NFM-PB-1 is 2.44, indicating that a greater proportion of Fe^{2+}_{LS} is involved in the energy storage process.

To further compare the differences in energy coupling effect between the conventional system (M-PB) and the NFM-PB system, the charge/discharge curves (100 mA/g) of the cathodes were investigated, as illustrated in Figure 2e. The unshaped coupling platform driven by water electrolysis is observed for M-PB after 25 cycles. However, the coupling platform of NFM-PB-1 can be vividly pointed out in the initial charge/discharge process, and does not undergo dramatic changes during 25 cycles. The discharge curves were transformed into dQ/dV profiles to precisely monitor the variations of discharge platform (Figure 2f). In the first cycle (0.1 C), a distinct boundary (3.43 V) is demarcated between the reduction peaks of $Mn^{2+}_{HS}/Mn^{3+}_{HS}$ and $Fe^{2+}_{LS}/$

Fe^{3+}_{LS} in M-PB, while only a broad reduction peak is found in the high-voltage region of NFM-PB-1 (Figure 2c). For M-PB, the reduction peaks of $Mn^{2+}_{HS}/Mn^{3+}_{HS}$ and $Fe^{2+}_{LS}/Fe^{3+}_{LS}$ are shifted by 0.14 V and 0.03 V towards lower voltages, respectively, as the current density increases from 10 mA/g to 100 mA/g. It is noteworthy that a new peak at 3.28 V appears, and on gradually intensified with an increase in the number of cycles. Simultaneously, the reduction peaks of $Mn^{2+}_{HS}/Mn^{3+}_{HS}$ and $Fe^{2+}_{LS}/Fe^{3+}_{LS}$ is gradually weakened and further shifted towards the new peak, which is related to the water electrolysis. Nevertheless, the coupling peak of M-PB is still not completely formed after 25 cycles. In addition, the intensity of its coupling peak in the 25th cycle is lower than that in the 15th cycle, due to the capacity degradation of the cathode. Interestingly, a pronounced energy coupling phenomenon in NFM-PB system is monitored during the initial charge/discharge process. The characteristic peaks of $Fe^{2+}_{HS}/Fe^{3+}_{HS}$ (0.16 V) and the coupling region (0.07 V) underwent varying degrees of polarization, with the increase of current density, which means that the coupling region displays superior anti-polarization property. Meanwhile, the electrochemical behavior of NFM-PB-1 is not significantly altered during 25 cycles, which indicates that a voltage can be steadily supplied in the structure-driven energy coupling platform. Moreover, the loss of capacity within the 25 cycles is primarily associated with $Fe^{2+}_{HS}/Fe^{3+}_{HS}$ (Figure S20), demonstrating an improved stability of the coupling platform.

To compare the polarization and diffusion of Na^+ in the coupling platform induced by different factors, the CV curves at different scan rates was measured (Figure S21) and the polarization of the Figure 2g. The first appearance of the energy coupling peaks at different scan rates was recorded in M-PB is detected at 0.4 mV/s, when the polarization is as high as 0.62 V, which is 2.82 times that of NFM-PB-1 (0.22 V). As the scan rate is increased from 0.4 mV/s to 1.0 mV/s, the polarization of M-PB is enhanced by 0.15 V, while NFM-PB-1 only changes by 0.08 V, highlighting the low polarization characteristics due to the structure-driven coupling behavior. In accordance with the Randles–Sevcik equation, there is a proportional relationship between D_{Na+} and the slope of the $I_P/\upsilon^{1/2}$ profile.[21] In comparison to M-PB, NFM-PB-1 performs a larger slope, indicating a faster Na^+ diffusion in the coupling platform (Figure 2h). CV measurements at 0.1 mV were conducted to further observe the evolution of energy coupling phenomenon induced by water electrolysis and confined element distribution, respectively. The evolution process of coupling effect is similar to the dQ/dV curves obtained under constant current conditions (Figure 2i).

Rate capability and cycling experiments were conducted to exploit the beneficial effects of the confined element strategy on prolonging the cycle life. As depicted in Figures 3a and S22, the influence of surface Ni enrichment is limited, while that of Fe is remarkable on improving the rate performance, when Ni or Fe are used individually. Nevertheless, the rate performance is considerably enhanced when Ni^{2+} and Fe^{2+} are introduced into the lattice simultaneously. At a high rate of 10 C, the discharge capacity of NFM-PB-1 still reaches 102.7 mAh/g, which is remarkably higher than that of M-PB (9.4 mAh/g). With the increased current density, more visible fluctuations in coulombic efficiency can be noticed for M-PB, compared to NFM-PB-1. Besides, the adverse effect of Ni^{2+} on the activity of Fe^{2+}_{HS} had been once again noted (Figure S22).

The apparent Na-ion diffusion rate was calculated depending on the galvanostatic intermittent titration technique test (GITT), as shown in Figures 3b and S23. The values of D_{Na+} for M-PB and NFM-PB-1 floats around 10^{-12} cm^2/s and 10^{-11} cm^2/s, respectively, indicating that the diffusion barrier of Na^+ is reduced by the confined element strategy. Consistent with the CV results, the relevant parameters of NFM-PB-1, including IR, ΔE_τ, and ΔE_S in localized region, are all smaller than those of M-PB, demonstrating a reduction of electrochemical polarization and Na^+ migration energy barriers.[22] DFT calculations were utilized to further investigated the improved rate performance. As Fe and Ni are introduced into the lattice, the energy band gap is gradually shortened, which facilitates the conduction of electrons (Figures S24 and S25). In addition, the energy barrier of Na^+ diffusion passing through the 24d site and moving along the *c*-axis was evaluated by DFT. As shown in Figure S26, the energy barrier that guest ions need to overcome in the NFM-PB-1 is lower, compared with M-PB.

The cycling stability of cathodes under the current density of 1 C and 5 C was recorded in Figures 3c–e, S27, and S28. Even at 1 C, the stability of the unmodified cathode is quite unsatisfactory, showing a specific capacity of 36.5 mAh/g (39.93 % retention) after 300 cycles. After repeated Na^+ (de)sodiation, NFM-PB-1 performs a final specific capacity of 102.3 mAh/g with an impressive capacity retention (87.64 %). Meanwhile, the NFM-PB-1 maintains a capacity retention of 85.19 % (91.1 mAh/g) after 1000 cycles at 5 C, while it is only 23.30 % for Mn-PB. Besides, the charge/discharge curves of cathodes in the first 100 cycle times were compared to study the electrochemical changes brought by the structural degradation. Except for the capacity decay, increasingly severe polarization is observed in M-PB, while the electrochemical behavior of NFM-PB-1 with confined element distribution is more stable (Figure 3d). Moreover, cycling and rate performance of the NFM-PB-1 cathode with non-uniform distribution is remarkable in PBAs-based SIBs (Figures S29 and Table S3). Full cells were assembled using PBAs as cathode and hard carbon (HC) as anode to evaluate the feasibility of the confined element strategy for practical applications. As shown in Figures S30–32, NFM-PB-1jj HC displays superior cycling performance (79.35 % capacity retention after 250 cycles at 100 mA/g) and rate performance (88.9 mAh/g at 1000 mA/g) compared to M-PBjj HC.

To unveil the structural essences behind the high capacity retention of NFM-PB-1, SEM was employed to observe the morphological changes of the cathodes before and after 300 cycles (Figure S33). Severe structural damage, including penetrating bulk cracks, partial surface microcracks, and structural collapse, can be observed in the region #1 of M-PB. In contrast, the initial dense morphology is retained for NFM-PB-1. Undoubtedly, Ni and Fe on the

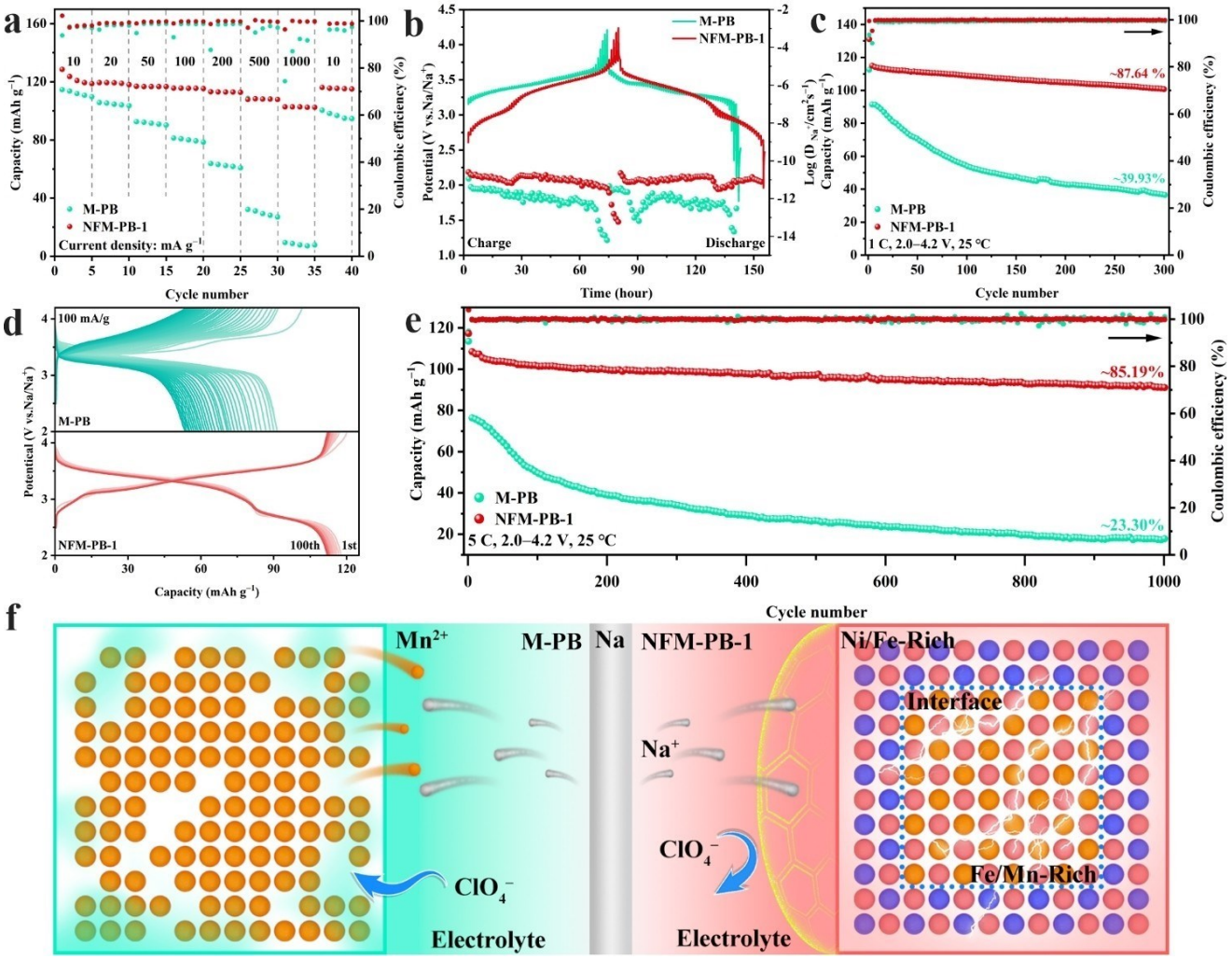

Figure 3. Electrochemical performance. a) Rate capacity. b) GITT curves and the calculated D_{Na+}. c) Cycling performance at 100 mA/g. d) Galvanostatic charge/discharge curves of different cycles. e) Long cycling performance at 500 mA/g. f) schematic illustration of confined element strategy on protection mechanism (The purple, pink, and yellow spheres represent Ni^{2+}, Fe^{2+}, and Mn^{2+} in the crystal, respectively).

surface heighten the cycling stability by strengthening the structure to inhibit stress release and minimizing the exposure of MnN_6 octahedra to avoid loss of active components, as depicted in the schematic illustration of the protection mechanism (Figure 3f). Furthermore, the Fe accompanying Mn plays a role in restraining the stress accumulation caused by distortion of the MnN_6 octahedra.

Ex situ Raman spectroscopy was employed to investigate the variation of the Fe–N–TM during the sodium ion (de)sodiation process. As depicted in Figure 4a, distinct alterations in the chemical environment surrounding the C–N is noticed, including the disappearance of Raman peaks corresponding to the ν(CN) bands and the emergence of a new peak at 2167 cm^{-1}.[23] Although these features are reversible, they also imply the drastic distortions of the Fe–C–N–Mn. For the NFM-PB-1, only a slight Raman red-shift is observed as the Fe–C–N TM is successfully reinforced by the confined element strategy. (Figure 4d). Besides, the differences of the Raman peaks between M-PB and NFM-PB-1 are closely related to the variations in coordinated atom of the C–N.

The mechanism of the phase transition for cathodes was further confirmed by in situ XRD measurements during the Na^+ (de)sodiation process. The maximum shift of diffraction peak (200) for M-PB and NFM-PB-1 is 0.43° and 0.19°, respectively, as shown in Figures 4b and 4e. Both cathodes underwent a reversible phase transition between cubic and tetragonal phase during charge/discharge process.[24] The lattice parameters were calculated based on the diffraction peak features (Figures 4c and 4f). The values of ~*c* for M-PB and NFM-PB-1 are 0.239 Å and 0.119 Å, respectively, indicating that a smaller lattice distortion is occurred in NFM-PB-1. Obviously, both the structural stability of the cathode and the volume expansion/contraction is optimized by the confined element strategy.

The redox mechanisms were analyzed by collecting XPS and XAS at several crucial discharging states (Figures 4g–j and S34–36). The energy storage mechanism of M-PB is well consistent with previous reports. The capacity before 3.5 V

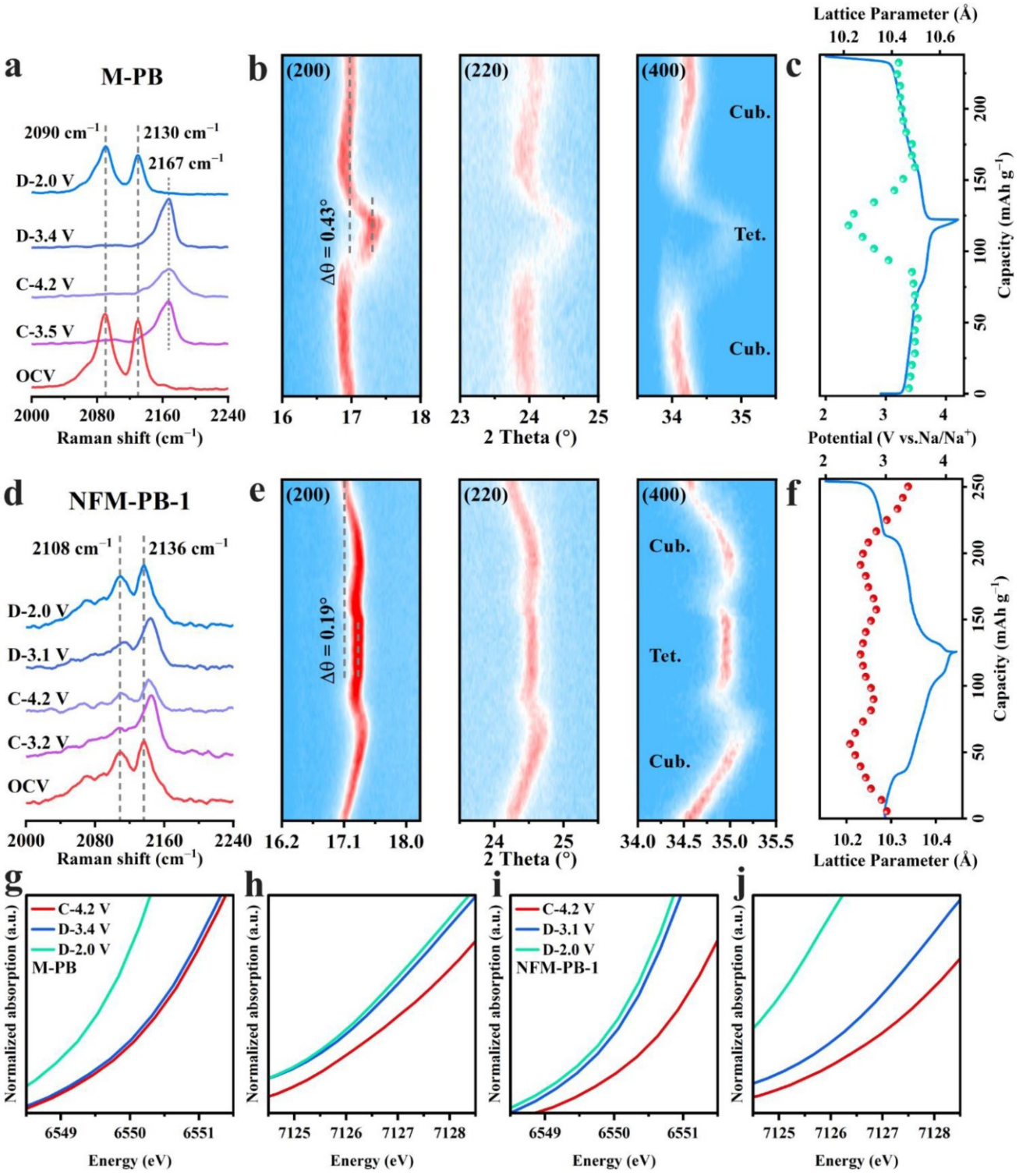

Figure 4. Charge compensation mechanism. Ex situ Raman spectra of (a) M-PB and (d) NFM-PB-1 at different states. In situ XRD pattern of (b) M-PB and (e) NFM-PB-1. The variation of *c*-axis during initial charge/discharge process for (c) M-PB and (f) NFM-PB-1. XAS spectra of (g) Mn K-edge and (h) Fe K-edge at different discharging states for M-PB. XAS spectra of (i) Mn K-edge and (j) Fe K-edge at different discharging states for NFM-PB-1.

is associated with the redox reaction of $Mn^{2+}{}_{HS}/Mn^{3+}{}_{HS}$, while the subsequent discharge capacity depends on the transition of $Fe^{2+}{}_{LS}/Fe^{3+}{}_{LS}$. For NFM-PB-1, the Fe absorption edge moves towards lower energy during the discharge process, which confirms the reduction reaction of Fe^{3+} throughout the discharge process (4.2–2.0 V, Figure 4j).

Meanwhile, the reduction of Mn^{3+} occurs concentratedly on the high-voltage platform (4.2–3.1 V). Evidently, the capacity within the range of 2.0–3.1 V is provided by $Fe^{2+}{}_{HS}$/$Fe^{3+}{}_{HS}$, while the capacity within other ranges is offered by $Mn^{2+}{}_{HS}$/$Mn^{3+}{}_{HS}$ and $Fe^{2+}{}_{LS}$/$Fe^{3+}{}_{LS}$. Apparently, the reactions of $Mn^{2+}{}_{HS}$/$Mn^{3+}{}_{HS}$ and $Fe^{2+}{}_{LS}$/$Fe^{3+}{}_{LS}$ were occurred simultaneously in the energy coupling platform.

Conclusion

In summary, inspired by the Irving-William order which revealed the transition metal ions sustained-release sequence, the confined element distribution at the M_1 site of PBAs was realized through forming a coordination competition relationship between chelators and $[Fe(CN)_6]^{4-}$ assisted by sodium citrate, synergistically inhibiting with localized enrichment and release of stresses originated from the Jahn–Teller effect, which is a novel application of adjustable composition property. As endorsed by theoretical calculations, the host element Mn^{2+}, the accompanied element Fe^{2+}, and the epitaxial element Ni^{2+} are sequentially dissociated from [TM-citrate] and then combined with $[Fe(CN)_6]^{4-}$, which contributed to a homogeneous cathode with non-uniform distribution of elements. As a result, chemically active Fe without Jahn–Teller effect is induced to accompany Mn, and zero-strain Ni is modulated to enrich at the particle surface, as clearly revealed by in situ XRD and ex situ Raman, remarkably suppressing the Jahn–Teller effect of MnN_6 octahedra and improving the cycling stability of cathodes. Compared with the traditional energy coupling effect caused by water electrolysis, the unconventional energy coupling effect, deriving from the confined element distribution, performs better electrochemical stability, anti-polarization, and guest ion transport ability, which is monitored by electrochemical measurements for the first time. Consequently, the optimized product (NFM-PB-1) demonstrates a high cycling retention of 85.19 % after 1000 cycles at 500 mA/g, and a superior rate capacity of 102.7 mAh/g at 1 A/g. The work demonstrates a cutting-edge case for adjustable composition property of PBAs, contributing to guiding the component design engineering for advanced PBAs.

Supporting Information

Supporting Information is available from the Wiley Online Library or from the author.

Acknowledgements

This work was financially supported by the National Natural Science Foundation of China (52325405, U21A20284, 52261135632), and the Fundamental Research Funds for Central Universities of Central South University (2024ZZTS0229). The authors thank the BL11B station in the Shanghai Synchrotron Radiation Facility (SSRF) and the U19 station in the National Synchrotron Radiation Laboratory (NSRL) for XAS measurements.

Conflict of Interest

The authors declare no conflict of interest.

Data Availability Statement

Research data are not shared.

Keywords: Confined Element Distribution · Irving-William Order · Energy Coupling Effect · Jahn–Teller Distortion · Prussian Blue Analogue Cathode

[1] a) J. Ge, L. Fan, A. M. Rao, J. Zhou, B. Lu, *Nat. Sustainability* **2022**, *5*, 225–234; b) K. Hurlbutt, S. Wheeler, I. Capone, M. Pasta, *Joule* **2018**, *2*, 1950–1960; c) Y. Tian, G. Zeng, A. Rutt, T. Shi, H. Kim, J. Wang, J. Koettgen, Y. Sun, B. Ouyang, T. Chen, Z. Lun, Z. Rong, K. Persson, G. Ceder, *Chem. Rev.* **2021**, *121*, 1623–1669; d) Y. Zeng, J. Xu, Y. Wang, S. Li, D. Luan, X. W. Lou, *Angew. Chem. Int. Ed.* **2022**, *61*, e202212031.

[2] a) M. Du, P. Geng, C. Pei, X. Jiang, Y. Shan, W. Hu, L. Ni, H. Pang, *Angew. Chem. Int. Ed.* **2022**, *61*, e202209350; b) W. Wang, Y. Gang, J. Peng, Z. Hu, Z. Yan, W. Lai, Y. Zhu, D. Appadoo, M. Ye, Y. Cao, Q.-F. Gu, H.-K. Liu, S.-X. Dou, S.-L. Chou, *Adv. Funct. Mater.* **2022**, *32*, 2111727; c) W. Jiang, T. Wang, H. Chen, X. Suo, J. Liang, W. Zhu, H. Li, S. Dai, *Nano Energy* **2021**, *79*, 105464; d) S. Chu, S. Guo, H. Zhou, *Chem. Soc. Rev.* **2021**, *50*, 13189–13235.

[3] a) X. Liu, Y. Cao, J. Sun, *Adv. Energy Mater.* **2022**, *12*, 2202532; b) J. Peng, M. Ou, H. Yi, X. Sun, Y. Zhang, B. Zhang, Y. Ding, F. Wang, S. Gu, C. A. López, W. Zhang, Y. Liu, J. Fang, P. Wei, Y. Li, L. Miao, J. Jiang, C. Fang, Q. Li, M. T. Fernández-Díaz, J. A. Alonso, S. Chou, J. Han, *Energy Environ. Sci.* **2021**, *14*, 3130–3140; c) H. Zhang, J. Peng, L. Li, Y. Zhao, Y. Gao, J. Wang, Y. Cao, S. Dou, S. Chou, *Adv. Funct. Mater.* **2023**, *33*, 2210725.

[4] a) X. Li, Y. Shang, D. Yan, L. Guo, S. Huang, H. Y. Yang, *ACS Nano* **2022**, *16*, 453–461; b) J. Sun, H. Ye, J. A. S. Oh, A. Plewa, Y. Sun, T. Wu, Q. Sun, K. Zeng, L. Lu, *Energy Storage Mater.* **2021**, *43*, 182–189; c) Z. Wang, M. T. Sougrati, Y. He, P. N. Le Pham, W. Xu, A. Iadecola, R. Ge, W. Zhou, Q. Zheng, X. Li, J. Wang, *Nano Energy* **2023**, *109*, 108256; d) H. Zhang, Y. Gao, J. Peng, Y. Fan, L. Zhao, L. Li, Y. Xiao, W. K. Pang, J. Wang, S.-L. Chou, *Angew. Chem. Int. Ed.* **2023**, *62*, e202303953.

[5] a) J. Liu, J. Liu, M. Tang, J. Fu, X. Kuang, J. Ma, *Adv. Funct. Mater.* **2024**, 2314167; b) J. Peng, J. Wang, H. Yi, W. Hu, Y. Yu, J. Yin, Y. Shen, Y. Liu, J. Luo, Y. Xu, P. Wei, Y. Li, Y. Jin, Y. Ding, L. Miao, J. Jiang, J. Han, Y. Huang, *Adv. Energy Mater.* **2018**, *8*, 1702856; c) B. Xie, P. Zuo, L. Wang, J. Wang, H. Huo, M. He, J. Shu, H. Li, S. Lou, G. Yin, *Nano Energy* **2019**, *61*, 201–210.

[6] J. Dai, S. Tan, L. Wang, F. Ling, F. Duan, M. Ma, Y. Shao, X. Rui, Y. Yao, E. Hu, X. Wu, C. Li, Y. Yu, *ACS Nano* **2023**, *17*, 20949–20961.

[7] a) Y. Ma, Y. Ma, S. L. Dreyer, Q. Wang, K. Wang, D. Goonetilleke, A. Omar, D. Mikhailova, H. Hahn, B. Breitung, T. Brezesinski, *Adv. Mater.* **2021**, *33*, 2101342; b) J. Peng, B. Zhang, W. Hua, Y. Liang, W. Zhang, Y. Du, G. Peleckis, S.

Indris, Q. Gu, Z. Cheng, J. Wang, H. Liu, S. Dou, S. Chou, *Angew. Chem. Int. Ed.* **2023**, *62*, e202215865; c) Y. Huang, X. Zhang, L. Ji, L. Wang, B. B. Xu, M. W. Shahzad, Y. Tang, Y. Zhu, M. Yan, G. Sun, Y. Jiang, *Energy Storage Mater.* **2023**, *58*, 1–8.

[8] Y. Shang, X. Li, J. Song, S. Huang, Z. Yang, Z. J. Xu, H. Y. Yang, *Chem* **2020**, *6*, 1804–1818.

[9] a) B. Xie, L. Wang, H. Li, H. Huo, C. Cui, B. Sun, Y. Ma, J. Wang, G. Yin, P. Zuo, *Energy Storage Mater.* **2021**, *36*, 99–107; b) F. Ma, Q. Li, T. Wang, H. Zhang, G. Wu, *Sci. Bull.* **2017**, *62*, 358–368; c) J. Peng, Y. Gao, H. Zhang, Z. Liu, W. Zhang, L. Li, Y. Qiao, W. Yang, J. Wang, S. Dou, S. Chou, *Angew. Chem. Int. Ed.* **2022**, *61*, e202205867.

[10] a) M. Jiang, Z. Hou, J. Wang, L. Ren, Y. Zhang, J.-G. Wang, *Nano Energy* **2022**, *102*, 107708; b) Y. Tang, L. Wang, J. Hu, M. Chen, M. Zhou, K. Wang, K. Jiang, *Adv. Energy Mater.* **2024**, *14*, 2303015; c) J. Peng, W. Zhang, Z. Hu, L. Zhao, C. Wu, G. Peleckis, Q. Gu, J.-Z. Wang, H. K. Liu, S. X. Dou, S. Chou, *Nano Lett.* **2022**, *22*, 1302–1310.

[11] a) Q. Wang, J. Li, H. Jin, S. Xin, H. Gao, *InfoMat* **2022**, *4*, e12311; b) W. Wang, Y. Gang, Z. Hu, Z. Yan, W. Li, Y. Li, Q.-F. Gu, Z. Wang, S.-L. Chou, H.-K. Liu, S.-X. Dou, *Nat. Commun.* **2020**, *11*, 980.

[12] L. Sacconi, A. Sabatini, *Nature* **1960**, *186*, 549–549.

[13] a) A. Choi, T. Kim, M.-H. Kim, S. W. Lee, Y. H. Jung, H.-W. Lee, *Adv. Funct. Mater.* **2022**, *32*, 2111901; b) F. Gebert, D. L. Cortie, J. C. Bouwer, W. Wang, Z. Yan, S.-X. Dou, S.-L. Chou, *Angew. Chem. Int. Ed.* **2021**, *60*, 18519–18526.

[14] a) C. Xu, Y. Ma, J. Zhao, P. Zhang, Z. Chen, C. Yang, H. Liu, Y.-S. Hu, *Angew. Chem. Int. Ed.* **2023**, *62*, e202217761; b) Y. Ma, Y. Hu, Y. Pramudya, T. Diemant, Q. Wang, D. Goonetilleke, Y. Tang, B. Zhou, H. Hahn, W. Wenzel, M. Fichtner, Y. Ma, B. Breitung, T. Brezesinski, *Adv. Funct. Mater.* **2022**, *32*, 2202372.

[15] W. Li, C. Han, W. Wang, Q. Xia, S. Chou, Q. Gu, B. Johannessen, H. Liu, S. Dou, *Adv. Energy Mater.* **2020**, *10*, 1903006.

[16] L.-L. Zhang, C. Wei, X.-Y. Fu, Z.-Y. Chen, B. Yan, P.-P. Sun, K.-J. Chang, X.-L. Yang, *Carbon Energy* **2021**, *3*, 827–839.

[17] a) B. Xie, B. Sun, T. Gao, Y. Ma, G. Yin, P. Zuo, *Coord. Chem. Rev.* **2022**, *460*, 214478; b) G. Du, H. Pang, *Energy Storage Mater.* **2021**, *36*, 387–408.

[18] Y. Wang, P. Meng, Z. Yang, M. Jiang, J. Yang, H. Li, J. Zhang, B. Sun, C. Fu, *Angew. Chem. Int. Ed.* **2023**, *62*, e202304229.

[19] a) J. Song, L. Wang, Y. Lu, J. Liu, B. Guo, P. Xiao, J.-J. Lee, X.-Q. Yang, G. Henkelman, J. B. Goodenough, *J. Am. Chem. Soc.* **2015**, *137*, 2658–2664; b) J. Wu, J. Song, K. Dai, Z. Zhuo, L. A. Wray, G. Liu, Z.-x. Shen, R. Zeng, Y. Lu, W. Yang, *J. Am. Chem. Soc.* **2017**, *139*, 18358–18364.

[20] a) B. Wang, Y. Han, X. Wang, N. Bahlawane, H. Pan, M. Yan, Y. Jiang, *iScience* **2018**, *3*, 110–133; b) A. Zhou, W. Cheng, W. Wang, Q. Zhao, J. Xie, W. Zhang, H. Gao, L. Xue, J. Li, *Adv. Energy Mater.* **2021**, *11*, 2000943.

[21] G. Ji, J. Wang, Z. Liang, K. Jia, J. Ma, Z. Zhuang, G. Zhou, H.-M. Cheng, *Nat. Commun.* **2023**, *14*, 584.

[22] J. Chen, H. Chen, S. Zhang, A. Dai, T. Li, Y. Mei, L. Ni, X. Gao, W. Deng, L. Yu, G. Zou, H. Hou, M. Dahbi, W. Xu, J. Wen, J. Alami, T. Liu, K. Amine, X. Ji, *Adv. Mater.* **2022**, *34*, 2204845.

[23] Y. Tang, W. Li, P. Feng, M. Zhou, K. Wang, Y. Wang, K. Zaghib, K. Jiang, *Adv. Funct. Mater.* **2020**, *30*, 1908754.

[24] Y. He, S. L. Dreyer, Y. Y. Ting, Y. Ma, Y. Hu, D. Goonetilleke, Y. Tang, T. Diemant, B. Zhou, P. M. Kowalski, M. Fichtner, H. Hahn, J. Aghassi-Hagmann, T. Brezesinski, B. Breitung, Y. Ma, *Angew. Chem. Int. Ed.* **2024**, *63*, e2023153.